Aalborg Universitet

AALBORG UNIVERSITY

A Decentralized Reliability-Enhanced Power Sharing Strategy for PV-Based Microgrids

Jang, Jiahui; Peyghami, Saeed; Coates, Colin ; Blaabjerg, Frede

A Decentralized Reliability-Enhanced Power Sharing Strategy for PV-Based Microgrids

Jiahui Jiang, Saeed Peyghami, *Member, IEEE,* Colin Coates, *Member, IEEE,* and Frede Blaabjerg, *Fellow, IEEE*

Abstract—Microgrid (MG) technologies facilitate reliable, efficient and economic operation of distributed resources such as photovoltaic (PV) and battery storage systems. The well-known droop method controls different sources in a MG to properly share power supply. However, utilizing the droop method poses two major challenges. Firstly, while the droop method can prevent converter over-loading, it cannot protect them from over-stressing, thus deteriorating system reliability. Secondly, operating a 100% renewable-based MG requires a supervisory unit to monitor and control energy flow for load-generation balance. However, the supervisory unit relies on communication systems which impacts overall system reliability by being exposed to single-point failures and cyber-attacks. This paper proposes a decentralized power sharing approach that restricts thermal damage of converter components to avoid over-stressing converters. The main goal is to improve overall system performance and reliability by appropriately sharing active and reactive power among different sources without using communication systems. The simulations and numerical analysis show that the proposed decentralized strategy will properly control the power and energy flow among different sources. Moreover, it prevents over-stressing converters, consequently enhancing the overall reliability of the MG. An experiment is also presented to demonstrate the effectiveness of the proposed decentralized control approach.

Index Terms—AC microgrid, decentralized control, power sharing, system-level reliability, thermal stress, droop control.

I. INTRODUCTION

THIS century has seen an unprecedented increase in renewable energy integration into electric grids. Renewable energy sources (RES), such as photovoltaic (PV) and wind turbines, are often equipped with energy storage systems (ESS) in islanded applications. These sources are recognised as distributed generation (DG) units, of which the location is flexible and geographically distributed. Microgrid (MG) technology provides an efficient, reliable and economic way to integrate DG units with the help of power electronic converters. However, converters are one of the main sources of failures in renewable applications [1], [2]. Their reliability performance has gained an increasing interest in recent years [3]–[5].

Reliability of power electronic converters has been studied at three levels, including component-level, converter-level and system-level [5]. At component-level, the reliability model of converter components, e.g. semiconductors, capacitors, etc.,

J. Jiang and C. Coates are with the School of Electrical Engineering and Computing, University of Newcastle, Callaghan NSW 2308, Australia. (Emails: jiahui.jiang@uon.edu.au, colin.coates@newcastle.edu.au)

S. Peyghami and F. Blaabjerg are with the Department of Energy Technology, Aalborg University, Aalborg 9220 Øst, Denmark. (Emails: sap@et.aau.dk, fbl@et.aau.dk)

can be developed in order to design and manufacture products with a desired reliability [6]. At converter-level, active thermal control for an individual converter can be performed for its lifetime extension [7]–[14]. These studies provide the reliability evaluation of a single grid-connected converter. The system-level reliability has to consider each individual converter as well as their mutual impact. In a MG, parallel-connected converters complement each other in supporting the load demand. The power sharing strategy impacts on the operational condition of each converter, and consequently its reliability.

Conventionally, the power sharing among parallel-connected converters in a MG employs the well-known droop method [15]. The droop method shares the load power among different sources proportionally to their rated power, which effectively protects the converters from over-loading [15]–[18]. However, implementing the conventional droop method poses two major issues to MGs. Firstly, the droop method cannot effectively avoid converter over-stressing because its thermal stress depends on both its power loading as well as operational and environmental conditions [19], [20]. For instance, some ambient temperature (T_a) fluctuations or a failure in the converter cooling system will change junction temperature (T_j) of the critical components, and hence, affect their thermal stresses. The over-stressing issue has been explored in DC MGs by presenting a reliability-oriented power sharing strategy in [20]. Unlike the constant droop gain in conventional droop method, the droop gains in [20] are updated monthly aiming to shift the active power from the high-stressed converters to the low stressed converters. This will extend the aging process of the converters and improve the overall system reliability. However, the proposed active power sharing pattern may overlook the constraints exposed by power sources, e.g. intermittent PV generation, and economic efficiency.

Secondly, in a 100% RES-based MG, a supervisory controller and communication systems are required due to the fluctuating and uncertain nature of renewable generation. This degrades the system reliability by being exposed to single-point failures, cyber-attacks, etc. These issues can be solved by autonomous RES and ESS coordination through modified droop control [21]–[25]. However, the reliability-oriented strategy in [20] relies on a central controller and communications because the converter thermal stresses are mainly induced by the slow dynamics in mission profiles. The central controller stores the historical data and distributes the updated droop gains for local controllers monthly through communication links.

This paper proposes a novel decentralized power sharing

strategy in AC MGs aiming to improve the system reliability. The strategy:

a) Manages both real and reactive power loading as each impacts on converter reliability.

b) Adjusts droop coefficients based on converter thermal stresses. Line frequency temperature variations are shown to have the dominant impact on thermal aging in converters [26]. Droop coefficients are determined locally at each source by on-line monitoring of line frequency thermal stresses, eliminating the need for intensive calculations or inter-unit communication.

c) Is applied in a PV-based MG where priority of supply is assigned to the renewable sources. This is in recognition of the increasing role PV plays in power systems. However, without losing generality, the proposed reliability-enhanced power sharing approach can be applied to any kind of AC MG.

The remainder of this paper is structured as follows. Section II presents the traditional power sharing algorithm and the reliability-enhanced power sharing strategy is proposed. In Section III, the decentralized control method is developed during the implementation of the proposed power sharing strategy. Simulations and numerical case studies are then presented in Section IV. Moreover, the capability of the proposed decentralized application is demonstrated by experiments in Section V. Finally, conclusions are drawn in Section VI.

II. POWER SHARING STRATEGIES IN A PV-BASED MG

This section overviews the hierarchical control strategy in a MG and focuses on the power sharing strategy at the primary level. The traditional power management in a PV-based MG is first demonstrated. It is then followed by a reliability-enhanced power sharing strategy which aims to improve system-level reliability by adjusting both real power and reactive power flows.

A. The Traditional Power Sharing in a PV-Based MG

The hierarchical control strategy is widely adopted in a MG, as shown in Fig. 1. It is composed of three levels: primary control, secondary control and tertiary control. The primary control is responsible for instantaneous power balance between generation and consumption in a decentralized manner. The secondary control can realize some optimal power management and also regulate grid voltage and frequency. Some advanced functions are applied to the tertiary level, e.g. load forecasting, generation prediction, demand side management and market participation. This paper discusses the real-time power sharing at primary level with the purpose of improving its performance and consequently overall reliability of the system.

An islanded MG is generally supported by DG units including RES, ESS and some conventional sources. Since this paper mainly discusses the reliability issue caused by the aging of power electronics, the proposed MG only integrates converter-based RES/ESS. The structure shown in Fig. 2 represents a MG supported by PV and battery units. In the MG with a high penetration level of PV, the main power generation
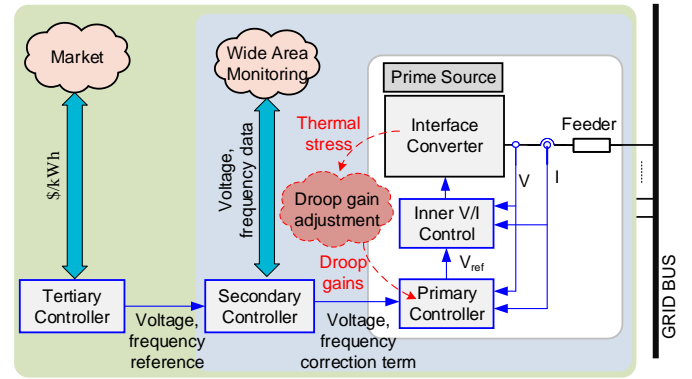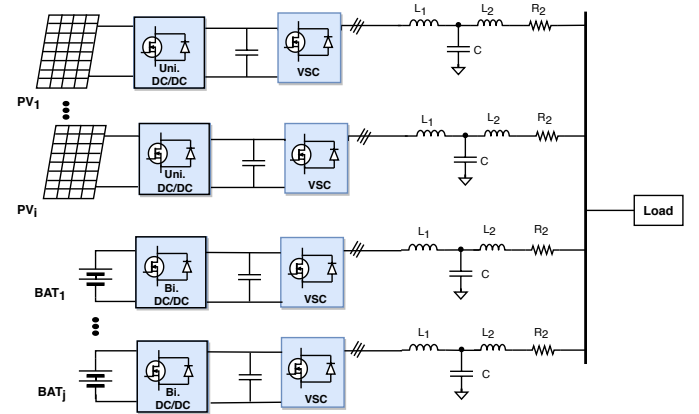

Fig. 1. Hierarchical control level of an AC MG

Fig. 2. Structure of a PV-based islanded MG with batteries (BAT: Battery; VSC: Voltage Source Converter)

is from PV panels. When the power demand is below the maximum available PV generation (P_{MPP}), the excess power can be stored into the interfaced batteries. However, the battery management system restricts its maximum charging rate, which may lead to necessary PV curtailment. On the other hand, when the PV generation under maximum power point tracking (MPPT) is not sufficient to support the power demand, the batteries release power to maintain power balance within the system. The details of battery management are demonstrated below.

To prolong the lifetime of a battery, the battery management should be carefully designed based on manufacturer's specifications. The maximum discharging rate P_{B-max} is restricted by a specified value P_{B0} from datasheet and it reduces to zero when the state of charge (SOC) level drops to a low threshold SOC_{low}, as demonstrated in (1). The standard charging rate P_{ch} also depends on the SOC. The charging mode transits to constant voltage charging from constant current charging after the SOC level reaches the reference value SOC_{ref}. The charging rate determination can be simplified to (2).

$$P_{B-max} = \begin{cases} P_{B0} & \text{if } SOC > SOC_{low} \\ 0 & \text{if } SOC \leq SOC_{low} \end{cases} \qquad (1)$$

$$P_{ch} = \begin{cases} P_{B0} & \text{if } SOC < SOC_{ref} \\ P_{B0}e^{-\frac{SOC-SOC_{ref}}{\delta SOC/k_\delta}} & \text{if } SOC \geq SOC_{ref} \end{cases} \quad (2)$$

where SOC_{ref} is the threshold where constant voltage charging starts; δSOC is the range over which constant voltage charging before the battery is fully charged; k_δ is a constant value determining the reduction speed of charging rate. Meanwhile, the SOC of battery can be estimated by an ampere-hour (Ah) counting method expressed below [27]:

$$SOC = SOC_0 + \int_0^t \frac{I_{BAT}(\tau)}{3600 C_{BAT}} d\tau \quad (3)$$

where SOC_0 represents the initial SOC, C_{BAT} is the capacity of the battery in Ah and I_{BAT} is charging current.

The power sharing within each type of power source (PV/battery) follows the principle of proportional sharing. That is to share the total power demand proportionally to the rated power of VSCs, which can be achieved by the droop method:

$$\omega_i = \omega_0 - m_i(P_i - P_0) \quad (4)$$
$$E_i = E_0 - n_i(Q_i - Q_0) \quad (5)$$

where P_i, Q_i are measured real and reactive power and P_0, Q_0 are reference real power and reactive power respectively; ω_i, E_i are reference values of VSC frequency and voltage respectively while ω_0, E_0 are the corresponding set point values; m_i and n_i are droop coefficients of real and reactive power respectively. The proportional sharing relies on the appropriate selection of droop coefficients, which is detailed in the following equations:

$$m_{pvi} = \frac{\Delta\omega}{pf \cdot S_i}, \quad i = 1, \ldots, u \quad (6)$$

$$m_{batj} = \frac{\Delta\omega}{pf \cdot S_j}\eta(1 - SOC_j + \epsilon), \quad j = 1, \ldots, v \quad (7)$$

where m_{pvi} and m_{batj} are the real power droop coefficients of the ith PV unit and jth battery unit respectively; S_i and S_j specify the corresponding apparent power rating of the VSC with a power factor of pf; u and v represent the number of PV and battery units in the system respectively; $\Delta\omega$ is the maximum allowed frequency deviation complying with grid codes. It is worth noting that the factor of $\eta(1 - SOC_j + \epsilon)$ in (7) aims to balance the SOC level of paralleled batteries and a small value of ϵ maintains this factor above zero.

As for reactive power sharing, (5) can realize the proportional sharing by employing droop coefficients as follows:

$$n_i = \frac{\Delta V}{Q_{maxi}}, \quad i = 1, \ldots, u + v \quad (8)$$

where Q_{maxi} is reactive power capacity of ith unit and ΔV is the acceptable voltage deviation range. As the converter capacity (S_i) is fixed, reactive power capacity varies with real power flow and it can be determined by:

$$Q_{maxi} = \sqrt{S_i^2 - P_i^2} \quad (9)$$

where P_i is the measured active power. This design considers the limited capacity of a converter, which prevents it from over-loading.

The achieved proportional sharing can be represented as:

$$P_{pvi} = \left(\frac{1}{m_{pvi}} \Big/ \sum_{i=1}^u \frac{1}{m_{pvi}}\right)P_{PV} \quad (10)$$

$$P_{batj} = \left(\frac{1}{m_{batj}} \Big/ \sum_{j=1}^v \frac{1}{m_{batj}}\right)P_{BAT} \quad (11)$$

$$Q_i = \left(\frac{1}{n_i} \Big/ \sum_{i=1}^{u+v} \frac{1}{n_i}\right)Q_L \quad (12)$$

where P_{pvi} and P_{batj} are real power outputs from the ith PV unit and jth battery unit respectively; P_{PV} and P_{BAT} are total power outputs from PV units and batteries across the system; Q_i is the reactive power output from the ith unit and Q_L is the total reactive power demand.

Figure 3 illustrates conceptually how the MG system operating condition (defined by the individual source's real and reactive power operating point) is determined on a cycle by cycle basis. The methodology considers the availability of PV generation and assigns priority to the renewable source. The method also considers constraints imposed by the battery management system. Importantly, the actual implementation is decentralized and does not require any inter-unit communication or supervisory system input. Individual sources infer system real and reactive power requirements through local voltage and frequency measurements. The detail of the decentralized implementation of the method is given in Section III. It can be seen that the proportional power management from (6) to (8) only considers the converter capacity, which overlooks its accumulated aging due to thermal damage. This issue is addressed by a proposed reliability-enhanced power sharing strategy in the next section.

B. The Proposed Reliability-Enhanced Power Sharing

As converter aging is closely related with its loading, the converter reliability can be improved by shifting some load away according to its aging due to thermal damage. In the MG with parallel-connected VSCs, power loading on individual converters varies due to their unique source characteristics. The discussed traditional power sharing strategy expects different thermal stresses on different VSCs, especially between PV VSC and battery VSC. Although real power loading has a dominant effect on converter aging, reactive power loading also affects the thermal performance in AC networks. The commonly used proportional reactive power sharing strategy can prevent the VSC from overloading but not over-stressing. It can thus be adjusted for the purpose of improving system reliability. The principle of the proposed strategy is to shift more reactive power load to the VSC with less thermal stress while relieving the VSC with more stress. This strategy can be achieved by modifying $Q - V$ droop gains since a higher gain corresponds to a smaller fraction of power loading. Equation (8) is thus modified into:

$$n_i^R = \alpha n_i + (1 - \alpha)n_0\left(\frac{D_i}{D_0}\right)^\lambda, \quad i = 1, \ldots, u + v \quad (13)$$

finally selected.

In practice, the mismatch of thermal stresses on parallel-connected PV/battery VSCs can be attributed to a range of conditions, e.g. types of IGBT/Diodes, SOC_0 level, T_a, and so on. These disturbances may hasten the aging of one particular battery VSC among all parallel-connected battery VSCs, which imposes difficulty in maintenance scheduling.

The reliability improvement from adjusted reactive power sharing can be trivial in case of high power factor loading conditions. Proportional real power sharing within the same type of units can also be adjusted aiming to effectively balance the thermal stresses. In order to maintain the coordination between PV and battery, the original total power output from PV units and battery units are maintained respectively. It means the droop gain adjustment in PV VSCs is separate from that in battery VSCs by choosing reference thermal damage values separately. The $P-\omega$ droop gains are modified based on (6),(7):

$$m_{pvi}^R = \alpha m_{pvi} + (1-\alpha)m_0(\frac{D_i}{D_{pv0}})^\lambda, \ i = 1,\ldots,u \quad (14)$$

$$m_{batj}^R = \alpha m_{batj} + (1-\alpha)m_0(\frac{D_j}{D_{bat0}})^\lambda, \ j = 1,\ldots,v \quad (15)$$

where m_0 is the reference value for $P-\omega$ droop gain; D_i, D_j are estimated VSC damage in the ith PV unit and jth battery unit respectively.

The thermal damage of a converter is accumulated over the operation period, which is attributed to both short-term and long-term thermal profiles. The details of thermal damage estimation is demonstrated in Appendix A. In AC grid operation, the $50 \ Hz$ thermal cycles are identified as the main source of thermal damage [26]. Considering only $50 \ Hz$ thermal cycles allows the on-line estimation of thermal damage which can be realized locally without intensive communication and calculation. The updating process in the ith unit is shown in Fig. 4. According to the lifetime model of semiconductor devices, (A.1), the damage caused by each $50 \ Hz$ thermal temperature swing can be calculated based on a lookup table. The aging due to accumulated $50 \ Hz$ thermal damage can then be estimated based on (A.2). It does not rely on a counting algorithm since the time period of a thermal swing caused by $50 \ Hz$ power flow is fixed, i.e. $10 \ ms$. After processing, the updated droop gains are then fed into the power sharing strategy as demonstrated in Fig. 3.

III. DECENTRALIZED IMPLEMENTATION APPROACH

As mentioned in Section II, the full decentralization of the proposed power sharing strategy needs to consider the uncertain nature of PV generation and loading profiles. This section demonstrates the coordinated PV and battery operation through a decentralized control method. It is based on the coordination of droop control, MPPT and battery management.

In order to maintain power balance between generation and consumption in a MG, PV operation mode switches between MPPT and power curtailment, while battery switches between charging and discharging modes. The PV units operate under grid-forming function when curtailing power
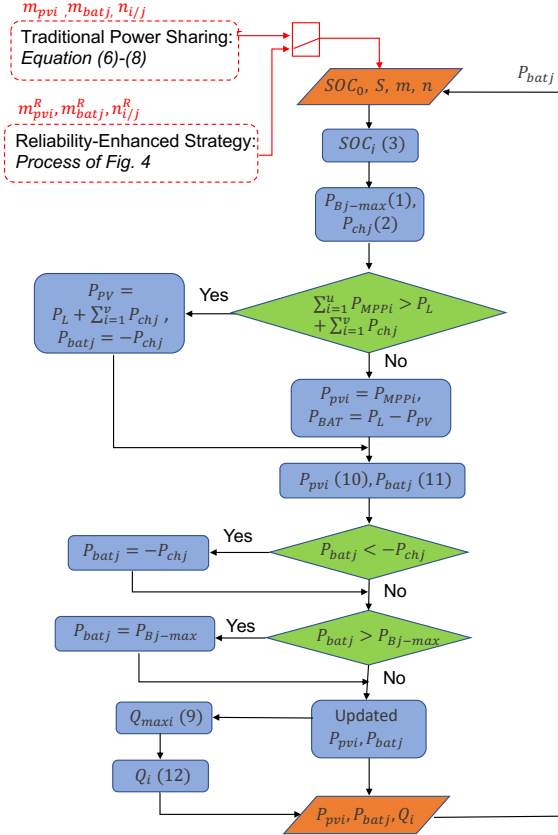

Fig. 3. System operation condition under the proposed power sharing algorithm in a PV-based MG

where n_0 is the reference value for $Q-V$ droop coefficient; D_i and D_0 are the estimated and reference value of accumulated VSC thermal damage in the ith unit, respectively. The weighting factor α allows a flexible adjustment between proportional sharing and reliability-enhanced sharing. If $\alpha = 1$, proportional power sharing is implemented and the impact of thermal damage is not considered. If $\alpha = 0$, the adaptive droop coefficient realises reliability-enhanced power sharing. In this paper, the α variable is used to switch between proportional and reliability-enhanced power sharing. It is envisaged that scenarios will exist where it would be appropriate to have some combination of both proportional and reliability-enhanced power sharing (e.g. a power system with several similarly aged/loaded sources might require those sources to proportionally share load amongst themselves while being collectively considered as a block in the context of reliability). The value of λ ($\lambda \geq 1$) tunes the speed of reactive power shifting as a result of thermal damage consideration. A higher λ can achieve quicker adjustment of the droop coefficient and thus quicker reactive power shifting. The effect of λ varies with system specifications but it can be designed with preliminary simulation studies based on the specific system configuration and various λ values. The λ value corresponding to the desired reactive power shifting performance can be

This article has been accepted for publication in a future issue of this journal, but has not been fully edited. Content may change prior to final publication. Citation information: DOI 10.1109/TPEL.2020.3040991, IEEE Transactions on Power Electronics

5
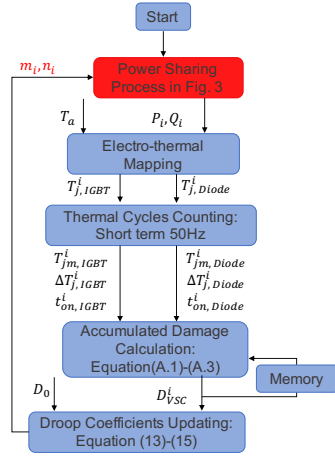

Fig. 4. The proposed process of droop gain adjustment for power sharing in an AC MG

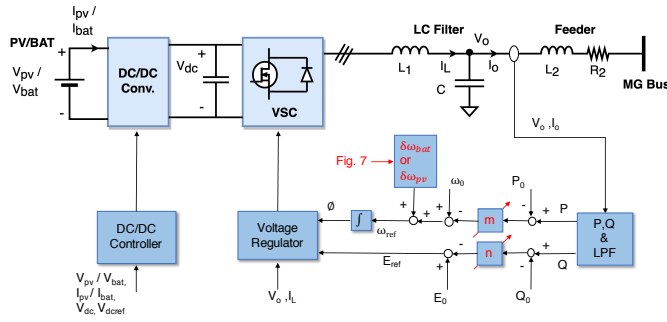Fig. 6. Modified droop method with grid-forming and grid-following functionalities

Fig. 5. Modified droop control in VSC: the generation of frequency adjustment term $\delta\omega$ ($\delta\omega_{bat}$ for battery and $\delta\omega_{pv}$ for PV) is shown in Fig. 7 and the controller for DC/DC converter is shown in Fig. 8
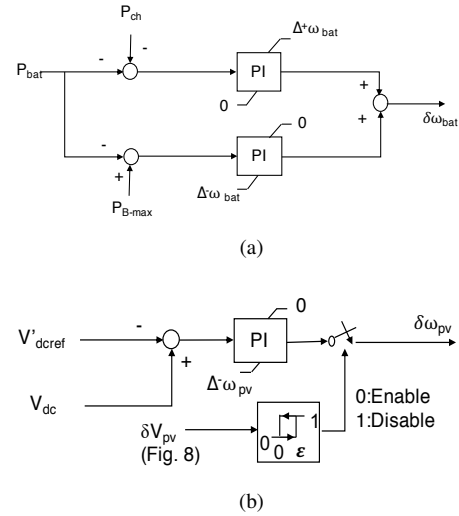
Fig. 7. Proposed frequency adjustment term $\delta\omega$ shown in Fig. 5 for (a) Battery and (b) PV

and operate under grid-following function when tracking the maximum power. The batteries operate as grid-following units when being charged at the standard rate and operate as grid-forming units in other conditions. The proposed decentralized control approach achieves the mode switching in the primary controller without relying on supervisory control or communication systems.

The decentralized approach is a modification of traditional droop method by imposing a term of $\delta\omega_i$ to the $P - \omega$ characteristics (4):

$$\omega_i = \omega_0 - m_i(P_i - P_0) + \delta\omega_i \tag{16}$$

The implementation diagram is shown in Fig. 5 based on the topology of a two-stage PV/battery source. The hardware implementation is shown in Fig. 21. The droop gains m and n are determined based on (6), (7), (8) in traditional power sharing and adjusted based on (14), (15), (13) in reliability-enhanced power sharing. The voltage controller is usually a double-loop control, which is composed of outer voltage control loop and inner current control loop. The details of the controller design can be found in [28].

The operating mode of a source is determined by the value of $\delta\omega_i$, which is demonstrated in Fig. 6. The unit operates in grid-forming mode along the droop portion of the characteristic while in grid-following mode along the vertical sections.
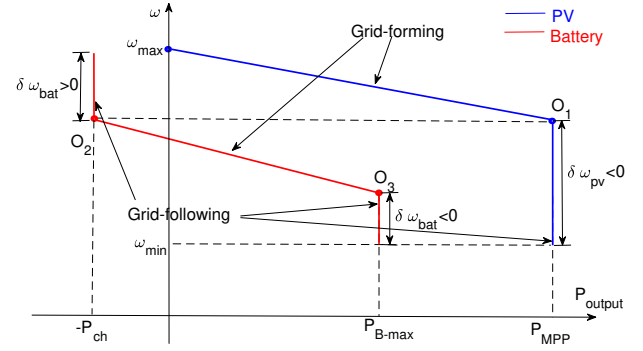
The droop section represents conventional droop method with zero $\delta\omega_i$. The vertical section at P_{MPP}/P_{B-max} achieves grid-following operation by imposing a negative $\delta\omega_{pv}/\delta\omega_{bat}$. The vertical section at $-P_{ch}$ limits the battery charging power with a positive $\delta\omega_{bat}$. The value of $\delta\omega_i$ is generated locally and it does not rely on I_r measurements in PV units (explained below).

In a battery unit, the upper and lower power limits, P_{B-max} and $-P_{ch}$, can be estimated based on (1),(2). The generation of $\delta\omega_{bat}$ can then be achieved by PI control, as shown in Fig. 7a. Meanwhile, the control of the buck-boost DC/DC converter in a battery source maintains load-generation power balance by regulating the DC bus voltage to a constant value.

Since the available PV power is varying and uncertain, the mode switching in PV operation cannot be achieved by traditional PI-controlled power limiting method. Instead, the dynamics of V_{dc} is used to indicate the condition of power balance between power generation from solar panels and power demand of the VSC. According to Fig. 7b, a negative $\delta\omega_{PV}$ will be generated when V_{dc} decreases after a power deficiency. It needs to be noted that this control loop is deactivated by a positive value (larger than ϵ to avoid impacts from noisy signals) of δV_{PV}. This signal is generated from the
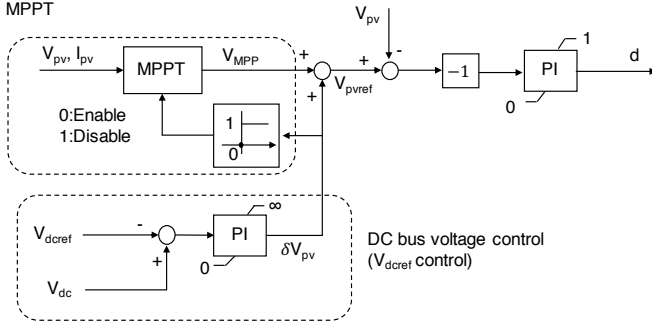
Fig. 8. Proposed control diagram of the PV DC/DC boost converter

TABLE I
PRIMARY CONTROL PARAMETERS IN SIMULATION

Parameters	Values	Parameters	Values
P_{0PV}	$10\ kW$	SOC_{low}	20%
P_{0BAT}	$-5\ kW$	SOC_{ref}	80%
$\omega_{0PV}/\omega_{0BAT}$	$314\ rad/s$	δSOC	10%
m_{PV}/m_{BAT}	$0.0001\ rad/(s\cdot W)$	k_δ	10
Q_{0PV}/Q_{0BAT}	$0\ Var$	SOC_{01}	50%
E_{0PV}/E_{0BAT}	$150\ V(rms)$	SOC_{02}	100%
n_{PV}/n_{BAT}	$0.002\ V/Var$	P_{B0}	$5\ kW$
V_{MPP}	$220\ V$	V_{dcref}	$410\ V$
V_{BAT}	$300\ V$	V'_{dcref}	$400\ V$

DC/DC boost converter controller and its diagram is shown in Fig. 8.

The DC bus voltage control in Fig. 8 maintains generation-consumption power balance with a PI controller on V_{dc}. It realizes PV power curtailment by generating a positive δV_{pv}. When in grid-following mode, δV_{pv} drops to zero which deactivates the $\delta\omega_{pv}$ generation loop and at the same time, MPPT loop comes into effect. Note that δV_{PV} serves as the switching signal between grid-forming and grid-following on both source side and VSC side.

IV. SIMULATION AND NUMERICAL ANALYSIS

The purpose of this section is to demonstrate the performance of the proposed power sharing strategy. Firstly, the effectiveness of the proposed decentralized controller is shown in short-term analysis and simulations. Then, the impact of the proposed power sharing approach in reliability enhancement is demonstrated by long-term simulation.

A. Short-Term Simulation

As shown in Fig. 2, the local load in the simulated MG is shared between PV and battery units. Assuming all PV units have the same power ratings and experience the same weather conditions, they are represented by a single PV unit in the system. The value of P_{MPP} is $9.5\ kW$ when $I_r = 1\ kW/m^2$ and $T_a = 25^oC$. In order to demonstrate the influence of SOC_0 on power sharing, two batteries with different SOC_0 levels are interfaced. Based on the control parameters presented in Table I, the power sharing performance is shown in Fig. 9 and Fig. 10.

It can be seen in Fig. 9 that PV source initially operates as a grid-forming unit when $I_r = 1\ kW/m^2$. It is under

power curtailment mode with $P_{pv} = 8\ kW$ corresponding to the local load ($P_L = 3\ kW$) and charging requirement for BAT1 ($P_{bat1} = -P_{B0} = -5\ kW$). BAT2 is charged at a rate of zero as it is initially fully charged. The PV source independently transitions to curtailment mode based on the value of its internal DC bus voltage. Rising DC bus voltage indicates excess generation. In this circumstance, the PV voltage is raised (δV_{pv}) above the maximum power point value (V_{MPP}) reducing the PV power generation (refer to Fig. 8).

I_r starts to decrease from $t = 2\ s$ and the PV switches to grid-following mode from $t = 2.5\ s$. At this point, the PV source transitions to MPPT mode as signified by the V_{PV} value aligning with $V_{MPP} = 220\ V$. The PV source is no longer able to meet the combined load and charging power requirement. In response, the charging rate of BAT1 drops below the standard charging rate P_{ch} under grid-forming operation.

During the $4\ s$ to $6\ s$ time interval, the system reaches steady state with the PV operating at its maximum power point ($P_{pv} = 5\ kW$) and the battery source charging at a reduced rate ($P_{bat1} = -2\ kW$), so that the local load ($P_L = 3\ kW$) continues to be supported. From $t = 6\ s$, an increase of local load ($P_L = 7\ kW$) exceeds the maximum available PV power ($P_{MPP} = 5\ kW$ under $I_r = 0.5\ kW/m^2$) such that two batteries start to discharge power ($P_{bat1} = P_{bat2} = 1\ kW$). They operate as grid-forming units while the PV perform grid-following function under this condition.

For simplicity, reactive power demand is designed to be shared equally among units and the droop coefficients m/n are set equal and constant. The mismatch of reactive power outputs from different units shown in Fig. 10 can be explained by voltage drop across the coupling line. Details can be seen in [29]. VSC output voltage and frequency behave as expected according to droop settings under the events shown in Fig. 9. The voltage magnitude drops after a reactive power demand increase at $t = 6\ s$ and frequency drops during transitioning periods. V_{dc} in PV operates at $V_{dcref} = 410\ V$ for the first $2\ s$ and drops to $V'_{dcref} = 400\ V$ during MPPT operation from $t = 2.5\ s$, which is as designed. V_{dc} in the batteries is relatively constant and smooth, which verifies the effective operation of the battery control.

The effectiveness of voltage regulation provided by the decentralized control strategy is verified by another simulation. The voltage output of BAT2 is simulated to experience a voltage sag due to some disturbances. The voltage drops by 30% at $t = 1\ s$ and it lasts for $0.2\ s$. The results in Fig. 11 have shown that the load voltage drop is mitigated to 9% by the other two VSC-based sources, i.e. PV and BAT1, injecting more reactive power to the grid. Note that the load voltage cannot restore back to the nominal value because a larger reactive power output causes a lower voltage reference under the droop method.

B. Long-Term Simulation

A numerical analysis is conducted based on the primary control strategy discussed in the last section. Although the
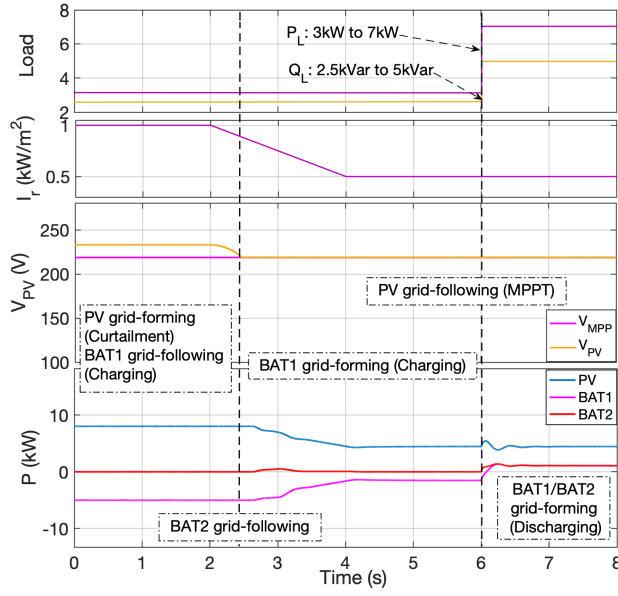
Fig. 9. Real power sharing and performance of PV operation at different operation modes

(a) Reactive power sharing

(b) VSC output voltage
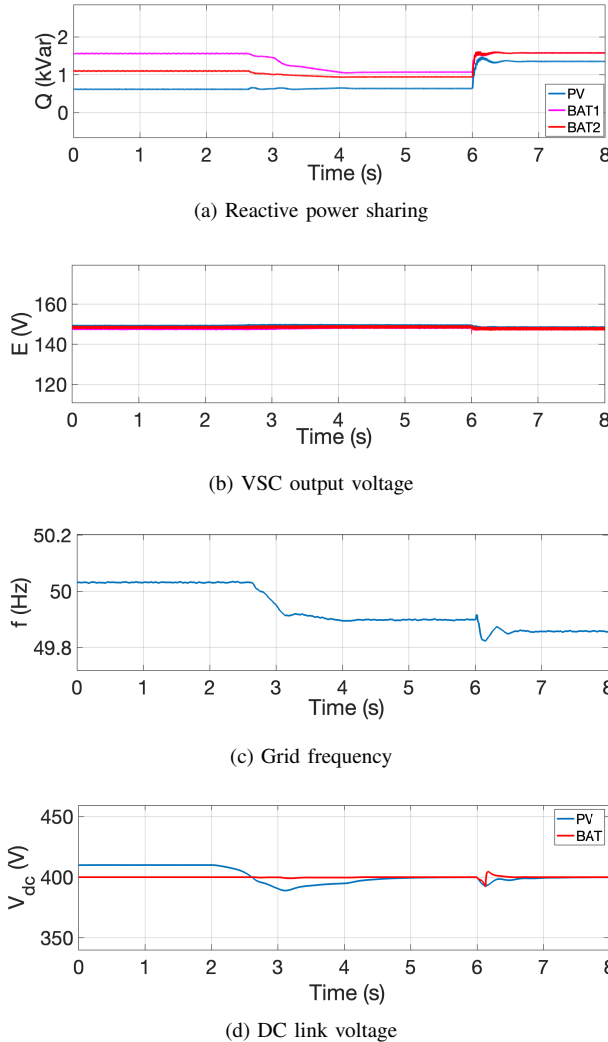

(c) Grid frequency

(d) DC link voltage

Fig. 10. Performance of the MG under the modified droop control
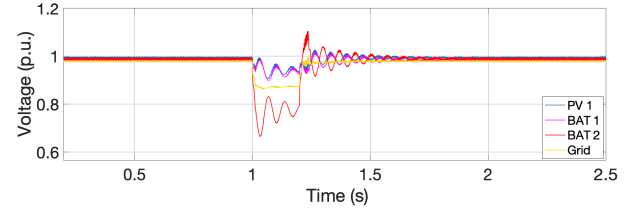

Fig. 11. Voltage regulation during a voltage sag

TABLE II
VSC SPECIFICATIONS IN NUMERICAL ANALYSIS

Parameters	VSC
Rated power	$5\ kW$
Switching frequency	$10\ kHz$
IGBT	IGB20N60H3
Diode	IDV15E65D2

proposed strategy is based on on-line adjustment, the reliability evaluation still needs to be based on long-term analysis because the thermal damage accumulates over the operation period. The simulated system in this section follows the MG structure as shown in Fig. 2. It is composed of three equivalent PV units and two batteries with the same capacity ($300\ Ah$). The interfacing VSCs are designed to be the same for each unit and the specifications are presented in Table II. The three-phase two-level topology is chosen for VSC such that each converter has six IGBT and six diodes. In theory, all IGBTs/Diodes in the VSC suffer from the same level of thermal stress such that we can focus on a single device here. During the operation, the SOC level of battery is monitored and follows the restrictions specified in Table I. The one-year mission profiles of a local hospital are shown in Fig. 12 with a sampling rate of one-minute. Note that the load profile is scaled down from practical data to accommodate to power sources in the designed MG. It is also assumed to have a constant power factor of 0.7. The sampling rate restricts the maximum update rate of droop coefficients in the reliability-enhanced power sharing strategy. The update rate in this simulation is set as every minute although it can be set at a slower rate to reduce computation burden.

1) Case 1 - Conventional Power Sharing: The yearly power sharing performance based on the strategy proposed in Section II is shown in Fig. 13. PV power output is closely related with I_r dynamics. Batteries are charged for most of the days when I_r is high and discharges at night to support local load. Since the system is islanded, batteries are supposed to maintain a high level of SOC in case of power shortages. However, the SOC levels of two batteries reduce dramatically during summer (from June to August), due to the high load demand after sunset. When the SOC level drops to SOC_{low}, load shedding or some backup sources (e.g. diesel generators) can be activated. However, these strategies are outside of the scope of this paper. Proportional reactive power sharing can also be seen in Fig. 13. The $Q-V$ droop coefficients are adaptive to its varying reactive power capacity, as shown in Fig. 13c. Reactive power is shared almost equally among these units, according to Fig. 13d. The weekly performance of real power outputs
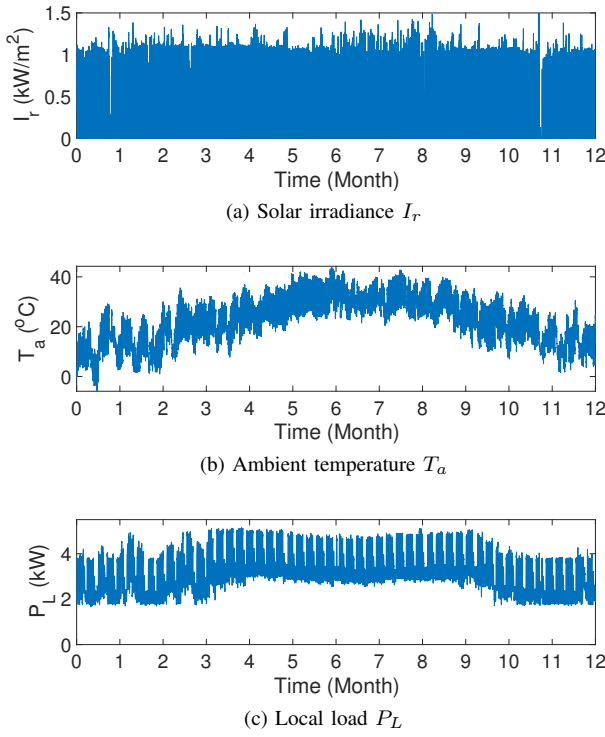
(a) Solar irradiance I_r

(b) Ambient temperature T_a

(c) Local load P_L

Fig. 12. One-year mission profiles used for assessing the MG

(a) Real power output from each PV unit

(b) Battery power output and SOC level

(c) $Q-V$ droop coefficients

(d) Reactive power outputs

Fig. 13. Performance of conventional power sharing in Case 1 for one year

from different units can be seen in Fig. 14. The circled part represents the period of PV power curtailment when battery charging rate is restricted under a high SOC level.

2) Case 2 - Reliability-Enhanced Reactive Power Sharing: The results shown in Case 1 have confirmed that power loadings on different VSCs are different, especially between PV VSC and Battery VSC. It is thus necessary to apply the novel reactive power sharing strategy to relieve thermal stresses on the VSCs, which suffer more thermal damage. In the reliability-enhanced power sharing strategy, the reference damage in (13) is chosen as $D_0 = D_{pv0} = D_{bat0} = \frac{0.1t}{525600}$ while $n_0 = 0.002$. Choosing $\alpha = 0$ realizes reliability-enhanced power sharing and $\lambda = 3$ is chosen to achieve a relatively fast response. The simulation results shown later verify that the reactive power shifting can be completed within the first week. The variation of droop coefficient n is shown in Fig. 15a. It can be seen that the value is adaptive to the corresponding VSC damage. Meanwhile, the adjusted reactive power performance in Fig. 15b shows that almost all of the reactive power demand has been shifted to PV units. This phenomenon can be explained by thermal damage analysis.

With parameters chosen as $A = 9.34e14$, $\alpha_1 = -4.416$, $\beta = 1290$, $\gamma = -0.3$, VSC thermal damage under $50\ Hz\ T_j$ swing can be calculated (refer to Appendix A). It is compared between proportional reactive power sharing in Case 1 and reliability-enhanced reactive power sharing. It can be seen in Fig. 16 that battery VSCs suffer more thermal stresses than PV VSCs. The slight difference between BAT1 and BAT2 can be explained by different initial SOC values as $SOC_{01} = 1$ and $SOC_{02} = 0$. As the adjusted strategy tries to shift reactive power load to PV units, the battery VSCs are relieved by around 15.4% of thermal damage. The improvement can
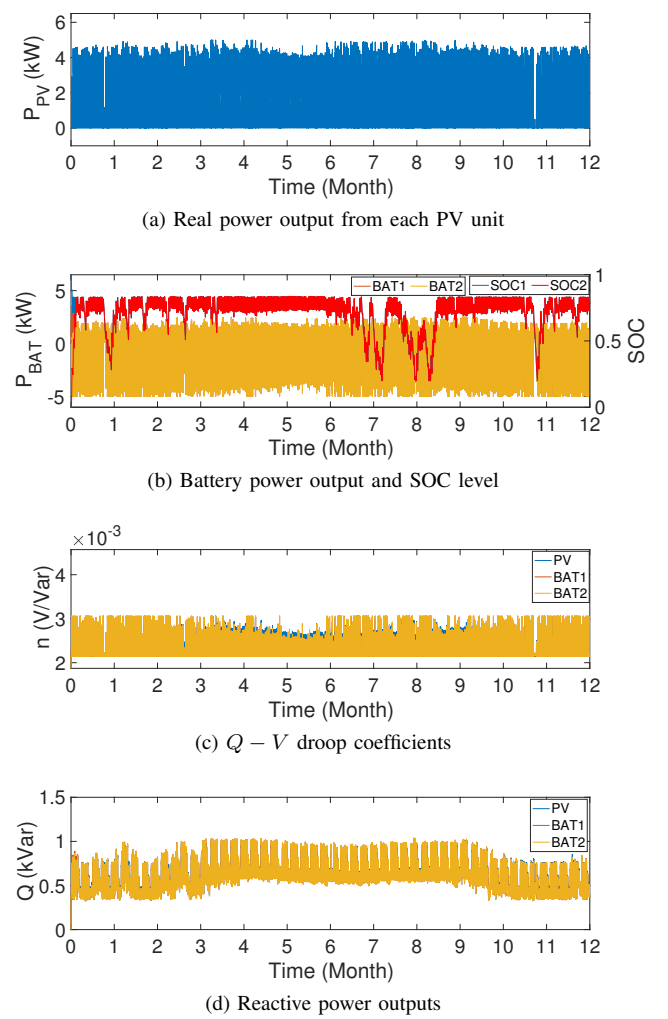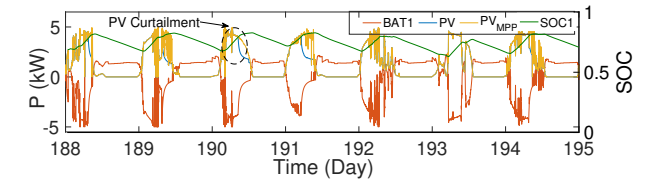

Fig. 14. Operating Conditions of PV and battery units in Case 1 for one week

also be seen in the lifetime performance based on Monte Carlo analysis [19]. The parameters in the device model and the lifetime model (A.1) are simulated under normal probability distribution function considering a 5% variation. The reliability of battery VSC is predicted according to [30], and shown in Fig.17 for both cases. It can be seen that the B1 lifetimes of battery VSC in Case 1 and Case 2 are around 26 years and 30 years respectively, which presents a 15.4% improvement.

3) Case 3 - Reliability-Enhanced Real/Reactive Power Sharing: Despite the reactive power sharing improvement, the mismatch on VSC thermal damage due to different SOC_0 between BAT1 and BAT2 has reduced minimally according
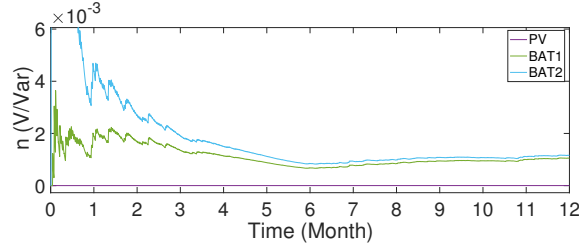
(a) Adjusted $Q - V$ droop gains n^R in (13)
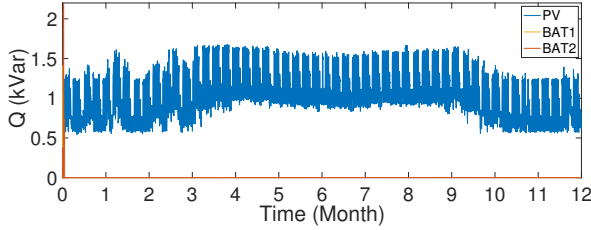
(b) Adjusted reactive power outputs

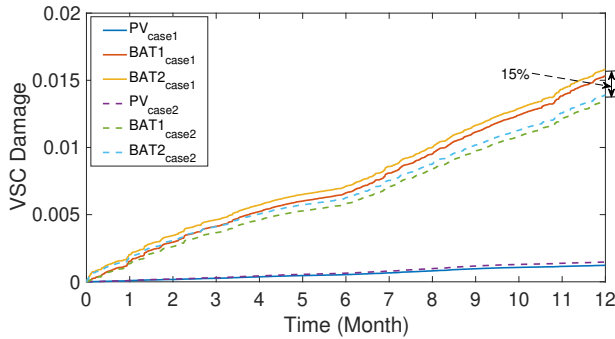Fig. 15. Performance of reliability-enhanced reactive power sharing in Case 2 for one year

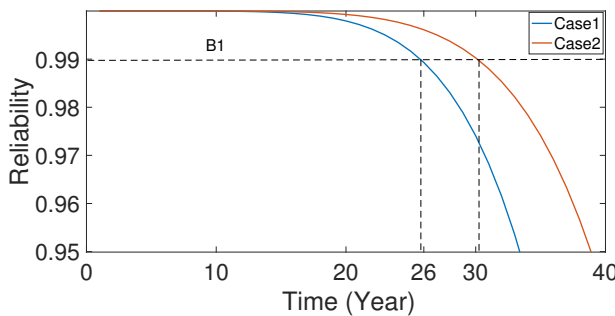Fig. 16. Accumulated thermal damage progression over one year (Solid: Case 1, Dash: Case 2

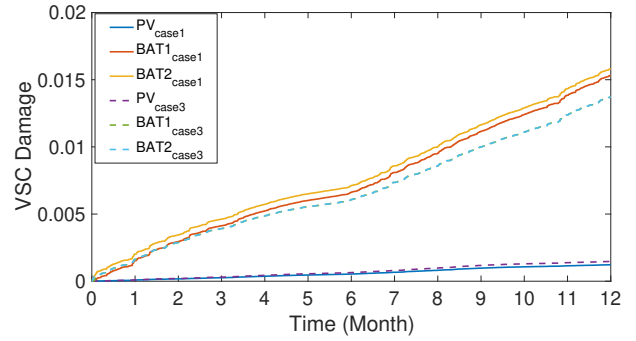Fig. 17. Reliability of the battery VSC in Case 1 and Case 2

Fig. 18. Accumulated thermal damage progression over one year with different SOC_0 (Solid: Case 1, Dash: Case 3)
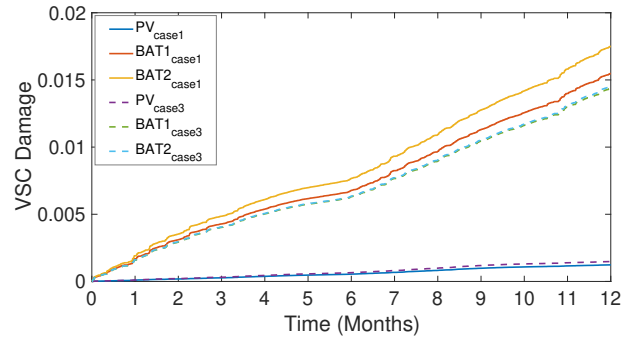

Fig. 19. Accumulated thermal damage progression over one year under different T_a (Solid: Case 1, Dash: Case 3)

to Fig. 16. It is because that the reactive power loading on parallel battery VSCs are almost equal and the thermal damage from reactive power loading is much less than that from real power loading. While different SOC_0 values cause around 4% difference in thermal damage, other factors may be more influential. For example, if a fan from the cooling system of the VSC in BAT2 has failed, the higher T_a will impose more thermal damage to the VSC in BAT2. Assuming a 10^oC difference in T_a, the thermal damage performance over one year operation is shown in Fig. 19. After applying the proposed reliability-enhanced control strategy in both real power and reactive power, the improvement can be seen in Fig. 18 and Fig. 19. The thermal damage on both battery VSCs decrease due to reactive power sharing adjustment. Meanwhile, the thermal damage mismatch between parallel-connected battery VSCs has also been reduced significantly, which is mainly due to the reliability-enhanced real power sharing adjustment.

4) Case 4 - Low-Frequency Reliability Updates: The thermal damage calculation so far has only considered the thermal damage caused by $50~Hz~T_j$ swing. In fact, there are low-frequency T_j swings over long-term operation. For example, the varying I_r causes daily swing in the VSC loading, which further results in daily T_j swings. The profile of local load attributes to weekly T_j swings. The rainflow counting algorithm is adopted here to obtain different low-frequency thermal cycles. The corresponding thermal damage can then be calculated and considered in power sharing algorithm.

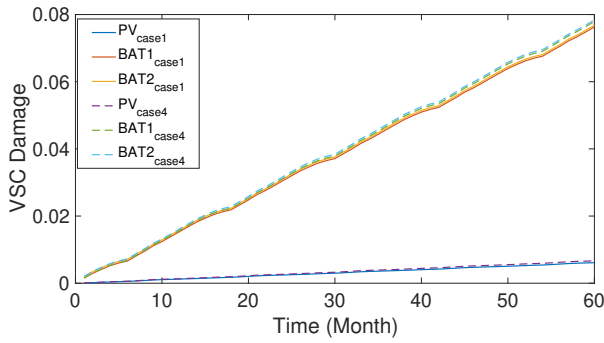Based on the same mission profiles, the thermal damage

Fig. 20. Accumulated thermal damage progression over five years (Solid: $50\ Hz$ thermal cycle; Dashed: Low-frequency included) in Case 4
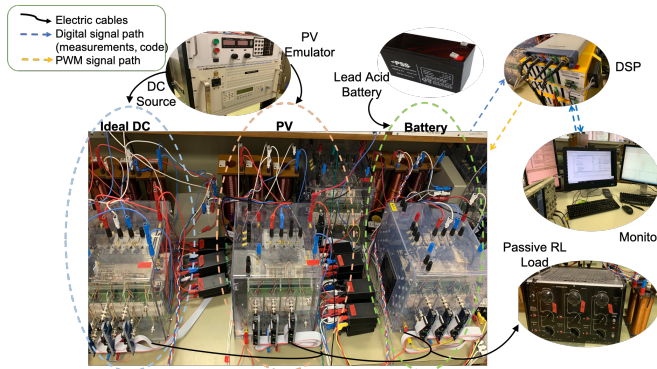

Fig. 21. Structure of the prototype MG

considering both $50\ Hz$ and low-frequency thermal cycles is shown in Fig. 20. Compared to that of $50\ Hz$ thermal cycles, the thermal damage of low-frequency cycles is very low, which is consistent with the findings in [19]. This phenomenon can be explained by the significantly low number of low-frequency thermal cycles experienced over a given time period relative to the number of $50\ Hz$ cycles. While the low-frequency thermal cycles can be associated with larger temperature variations, the impact is offset by the significantly lower number of these cycles experienced. It is thus reasonable to neglect the contribution of low-frequency thermal cycles for the purpose of power sharing improvement. It means droop coefficients can be updated as quick as $50\ Hz$ without analysing T_j profiles over long-term. Another advantage of this simplification is that the capacity requirement of the controller for memory storage and intensive calculation is significantly reduced as it is not necessary to store the mass operation data.

V. EXPERIMENTAL RESULTS

This section demonstrates the capability of the decentralized control method in power sharing without using communication systems. It provides experimental results conducted on a prototype MG as shown in Fig. 21.

Compared to the MG structure shown in Fig. 2, the prototype MG is only composed of one PV unit, one lead-acid battery and one backup power source (in case of power shortage). The specifications of the system components are listed in Table B.1 in Appendix B. The PV unit is emulated by Magna-Power

TSD600-8/+415HS and the maximum available power is set to $P_{MPP} = 850W$. In order to verify the effectiveness of the proposed battery management strategy, the battery limits are set to $P_{ch} = 100W$ and $P_{B-max} = 500W$ despite the actual battery capacity. The backup power is an ideal DC source which has no power limits. It is configured as a programmable AC generator connecting with a front-end rectifier. These three DC power sources connect to the MG through DC/AC converters, which is provided by SEMITEACH 18kW three-phase inverter. The system load is a passive RL load type which experiences several steps of change during the whole process. The control of interfaced converters is determined in a digitial signal processor (DSP). The detailed parameters in the modified droop control are listed in Table B.2.

The system performance is shown in Fig. 22. In Fig. 22(a), the PV unit real power output is $700W$ during the first 10s, which is below P_{MPP}. It operates at power curtailment mode and its DC link voltage is at $V_{dcref} = 360V$, as shown in Fig. 22(d). During this period, the battery is being charged under the standard rate of $-100W$ as a grid-following unit. At $t = 0\ s$, the load increases, which drives the PV unit to operate at MPPT mode and the battery charging rate drops. The V_{dc} in PV drops to the second reference value $V'_{dcref} = 320V$. During $t = 30\ s$ to $t = 40\ s$, the battery output reaches its upper limit such that the backup source starts to discharge. The reactive power demand experiences two steps changes at $t = 0\ s$ and $t = 70\ s$. The average reactive power sharing is designed for the three converters. The discrepancy shown in Fig. 22(b) is attributed to voltage drop across the coupling line, which is explained in [29]. The grid frequency in Fig. 22(c) decreases after every increase in real power load and increases after every decrease in real power demand, the value of which is determined by the droop settings.

The conducted experiment verifies the efficacy of the proposed decentralized implementation approach. It achieves the coordination of PV and battery in an islanded MG without relying on I_r sensors, inter-unit communication or a supervisory controller. The verified power sharing algorithm is based on traditional power sharing. However, the reliability-enhanced power sharing can also be applied after building the reliability model for the interfaced converters.

VI. CONCLUSIONS

This paper explores the restrictions of droop control in PV-based MG operation. Proportional droop control can effectively protect the interfacing converters from over-loading but over-stressing issue may still occur. The converter under more thermal stresses is more prone to fail which affects the system reliability. The proposed reliability-enhanced power sharing strategy adjusts both real power sharing and reactive power sharing for the purpose of improving overall system reliability. The principle is to reduce power loading on the converter with higher thermal damage. As a result, the lifetime of the most damaged converter can be extended. The implementation of the proposed power sharing strategy was via decentralized primary control. It is realized by modifying traditional droop control which avoids a supervisory controller and extensive communication links.
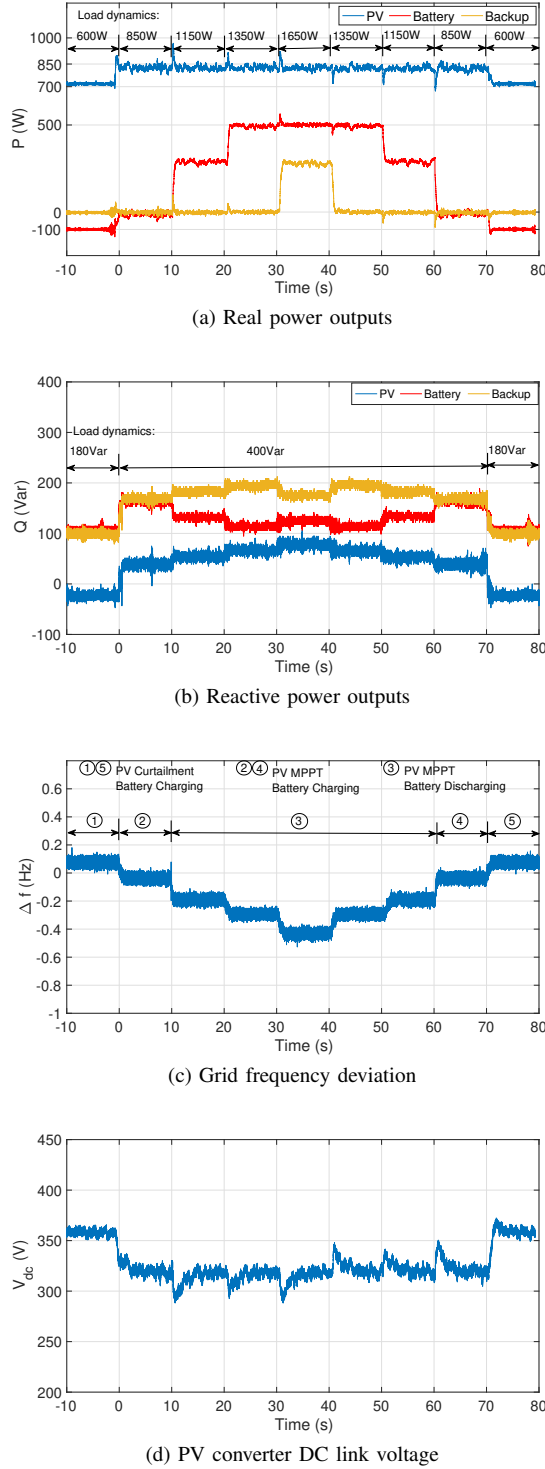
The performance of primary control was illustrated in a short-term simulation and hardware experiments. The switching between grid-following operation and grid-forming operation on both PV and battery units shows the effectiveness of the decentralized control approach. In addition, the reliability improvement was verified by a numerical analysis based on long-term mission profiles. In the simulated system, battery VSCs suffer from more thermal damage than PV VSCs. The majority of reactive power load is thus shifted to PV units under reliability-enhanced power sharing strategy. It contributes up to a 15.4% lifetime improvement in battery VSCs. The thermal damage can also be balanced for parallel-connected VSCs with different initial SOC_0 values and different T_a conditions. It is worth mentioning that although the proposed strategy is analysed in an islanded PV-based MG, it can be generalized for any converter-dominated AC systems. In future work, the thermal damage on DC link capacitor and DC/DC converters in the two-stage power sources can be included in the thermal damage estimation.

APPENDIX A
RELIABILITY MODELLING OF A CONVERTER

The lifetime consumption of a converter can be identified based on its lifetime model combined with temperature monitoring. Without losing accuracy, the calculation of thermal damage on a converter usually focuses on the most vulnerable components. It is acknowledged that semiconductor devices are critical components in the converter reliability assessment [6]. The thermal damage on semiconductors is thus used as the indicator of converter reliability in this paper. The junction temperature swing (ΔT_j) is critical to their lifetime [7]. According to [31], the lifetime model of semiconductor devices, insulated-gate bipolar transistor (IGBT) and diode, can be represented by its number of cycles to failure (N), as shown in (A.1).

$$ N = A \cdot \Delta T_j^{\alpha} \cdot exp(\frac{\beta}{T_{jm} + 273.15})t_{on}^{\gamma} \qquad (A.1) $$

where T_{jm} and ΔT_j represent minimum junction temperature and temperature swing of the cycle, respectively; t_{on} is the heating time; A, α, β, and γ are constants obtained from long-term lifetime tests. The aging of the device can then be calculated based on its thermal cycling:

$$ D = \sum_t \frac{n_t}{N_t} \qquad (A.2) $$

where D is the thermal damage of the device under n_t thermal cycles during operation period of t. N_t is the number of cycles to failure derived from (A.1) under the corresponding thermal cycle with T_{jm}, ΔT_j, and t_{on}.

As IGBT and diode have different thermal performances, the thermal damage on each device needs to be calculated separately. The total thermal damage on a VSC can then be represented by:

$$ D_{VSC} = max\{D_{g_T}^{(T)}, D_{g_D}^{(D)}\}, \qquad (A.3) $$

where $g_T \in \{1, ..., M^{(T)}\}$, $g_D \in \{1, ..., M^{(D)}\}$ and $M^{(T)}$, $M^{(D)}$ are numbers of IGBT and diodes in each VSC; $D_{g_T}^{(T)}$

Fig. 22. Obtained experimental results showing the performance of the proposed decentralized power sharing in the prototype MG

(a) Real power outputs

(b) Reactive power outputs

(c) Grid frequency deviation
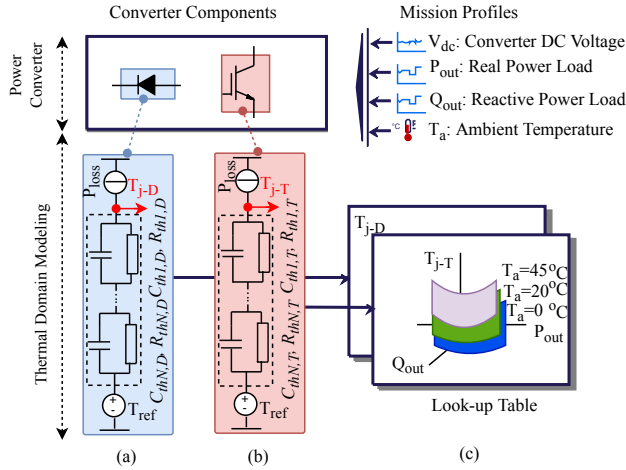
(d) PV converter DC link voltage

Fig. A.1. The procedure of electro-thermal mapping in the power converter: (a) Diode (b) IGBT (c) Look-up Table

and $D_{g_D}^{(D)}$ represent the thermal damage on a single IGBT and diode respectively in the discussed VSC.

The thermal performance of a converter during operation can be attained from electro-thermal mapping procedure [20] or direct temperature measurements [32]. It is not common to install temperature sensors in every DG because of the extra cost. In electro-thermal mapping, as shown in Fig. A.1, the thermal model of IGBT and diode should first be established. It includes parameters for thermal impedances, turn on-off switching energy, and V-I curves when conducting. Power losses on devices dissipate through their thermal impedances, which causes junction temperature increase. The steady-state junction temperature is mainly dependent on the thermal resistance R_{th} while its dynamic behaviour is mostly dependent on thermal capacitance C_{th}. These values can be obtained from the component datasheet and imported into a simulation platform, PLECS. The behaviour of T_j under a certain operating condition is automatically calculated by PLECS. As the power sources connect to the system in the two-stage form, the DC link voltage is relatively constant. VSC loading and ambient temperature thus become the main concerns of the operating conditions. The junction temperatures are stored in a look-up table for each component under different operating conditions. It can then be recalled when creating T_j profiles under specified mission profiles.

Once T_j profiles of every devices are created, the VSC thermal damage can be derived based on (A.1) to (A.3). Thermal cycles over a long operation period include both short-term cycles and long-term cycles. It is assumed that short-term cycle is equivalent to $50\ Hz$ cycle in AC grid. Long-term cycles are dependent on mission profiles, such as I_r, T_a and P_L. A cycle counting algorithm, called rain flow counting, can convert the randomly changed T_j profile into categorized thermal cycles. It identifies all the long-term thermal cycles existing in the temperature profile and extracts parameters for each thermal cycle, i.e. T_{jm}, ΔT_j, t_{on} and n_t [33]. The thermal damage on a component is the sum of thermal damage from all thermal cycles according to (A.2).

TABLE B.1
SYSTEM PARAMETERS OF THE PROTOTYPE MG

Hardware	Type
PV Emulator	Magna TSD600-8/+415HS
Battery	Lead-acid
Backup	California Instruments 4500Lx-400
VSC	SEMITEACH 18kW 3-ph Inverter
Boost Converter	SEMITEACH 18kW 3-ph Inverter
Buck-Boost Converter	SEMITEACH 18kW 3-ph Inverter
LC Filter	$2\ mH \& 20\ \mu F$
Line Inductor	$5\ mH$
DSP	TMS320F28377D

TABLE B.2
PRIMARY CONTROL PARAMETERS IN EXPERIMENTS

Parameters	Values	Parameters	Values
	PV	Battery	Backup Source
$P_0(W)$	900	-100	-600
$Q_0(Var)$	0	0	0
$P_{max}(W)$	850	500	850
$P_{min}(W)$	0	-100	0
$\omega_0(rad/s)$	314	314	314
$E_0(V)$	100	100	100
$m(rad/(s \cdot W))$	0.0005	0.00005	0.00005
$n(V/Var)$	0.005	0.005	0.005
$V_{dcref}(V)$	360	360	360
$V'_{dcref}(V)$	320	-	-

APPENDIX B
SPECIFICATIONS OF EXPERIMENTAL PROTOTYPE MG

In this section, the parameter details of the prototype MG are listed. Table B.1 shows the type of the system parts while Table B.2 lists the selection of primary control parameters.

REFERENCES

[1] L. M. Moore and H. N. Post, "Five years of operating experience at a large, utility-scale photovoltaic generating plant," *Progress in Photovoltaics: Research and Applications*, vol. 16, no. 3, pp. 249–259, 2008.

[2] M. Wilkinson, B. Hendriks, and P. Tavner, "Report on wind turbine reliability profiles," *GL-GH for Reliawind FP7-ENERGY-2007-1-RTD Deliverable D-1*, vol. 3, 2011.

[3] Y. Song and B. Wang, "Survey on reliability of power electronic systems," *IEEE Transactions on Power Electronics*, vol. 28, no. 1, pp. 591–604, 2012.

[4] F. Blaabjerg, Y. Yang, D. Yang, and X. Wang, "Distributed power-generation systems and protection," *Proceedings of the IEEE*, vol. 105, no. 7, pp. 1311–1331, 2017.

[5] S. Peyghami, P. Palensky, and F. Blaabjerg, "An overview on the reliability of modern power electronic based power systems," *IEEE Open Journal of Power Electronics*, vol. 1, no. 1, pp. 34–50, 2020.

[6] H. Wang, M. Liserre, F. Blaabjerg, P. de Place Rimmen, J. B. Jacobsen, T. Kvisgaard, and J. Landkildehus, "Transitioning to physics-of-failure as a reliability driver in power electronics," *IEEE Journal of Emerging and Selected Topics in Power Electronics*, vol. 2, no. 1, pp. 97–114, 2013.

[7] F. Blaabjerg, K. Ma, and D. Zhou, "Power electronics and reliability in renewable energy systems," in *2012 IEEE International Symposium on Industrial Electronics*. IEEE, 2012, pp. 19–30.

[8] K. Ma and F. Blaabjerg, "Modulation methods for neutral-point-clamped wind power converter achieving loss and thermal redistribution under low-voltage ride-through," *IEEE Transactions on Industrial Electronics*, vol. 61, no. 2, pp. 835–845, 2013.

[9] Z. Qin, M. Liserre, F. Blaabjerg, and H. Wang, "Energy storage system by means of improved thermal performance of a 3 mw grid side wind power converter," in *IECON 2013-39th Annual Conference of the IEEE Industrial Electronics Society*. IEEE, 2013, pp. 736–742.

This article has been accepted for publication in a future issue of this journal, but has not been fully edited. Content may change prior to final publication. Citation information: DOI 10.1109/TPEL.2020.3040991, IEEE Transactions on Power Electronics

13

[10] K. Ma, M. Liserre, and F. Blaabjerg, "Reactive power influence on the thermal cycling of multi-MW wind power inverter," *IEEE Transactions on Industry Applications*, vol. 49, no. 2, pp. 922–930, 2013.

[11] Y. Yang, H. Wang, and F. Blaabjerg, "Reactive power injection strategies for single-phase photovoltaic systems considering grid requirements," *IEEE Transactions on Industry Applications*, vol. 50, no. 6, pp. 4065–4076, 2014.

[12] A. Anurag, Y. Yang, and F. Blaabjerg, "Thermal performance and reliability analysis of single-phase pv inverters with reactive power injection outside feed-in operating hours," *IEEE Journal of Emerging and Selected Topics in Power Electronics*, vol. 3, no. 4, pp. 870–880, 2015.

[13] M. Andresen, G. Buticchi, and M. Liserre, "Study of reliability-efficiency tradeoff of active thermal control for power electronic systems," *Microelectronics Reliability*, vol. 58, pp. 119–125, 2016.

[14] S. Peyghami, P. Davari, H. Wang, and F. Blaabjerg, "The impact of topology and mission profile on the reliability of boost-type converters in pv applications," in *2018 IEEE 19th Workshop on Control and Modeling for Power Electronics (COMPEL)*. IEEE, 2018, pp. 1–8.

[15] J. Rocabert, A. Luna, F. Blaabjerg, and P. Rodríguez, "Control of power converters in ac microgrids," *IEEE Transactions on Power Electronics*, vol. 27, no. 11, pp. 4734–4749, 2012.

[16] M. M. A. Abdelaziz, "Effect of detailed reactive power limit modeling on islanded microgrid power flow analysis," *IEEE Transactions on Power Systems*, vol. 31, no. 2, pp. 1665–1666, 2015.

[17] A. Milczarek, M. Malinowski, and J. M. Guerrero, "Reactive power management in islanded microgrid—proportional power sharing in hierarchical droop control," *IEEE Transactions on Smart Grid*, vol. 6, no. 4, pp. 1631–1638, 2015.

[18] S. Peyghami, H. Mokhtari, and F. Blaabjerg, "Distributed and decentralized control of dc microgrids," *Dc Distribution Systems and Microgrids*, pp. 23–42.

[19] P. D. Reigosa, H. Wang, Y. Yang, and F. Blaabjerg, "Prediction of bond wire fatigue of igbts in a pv inverter under a long-term operation," *IEEE Transactions on Power Electronics*, vol. 31, no. 10, pp. 7171–7182, 2015.

[20] S. Peyghami, P. Davari, and F. Blaabjerg, "System-level reliability-oriented power sharing strategy for dc power systems," *IEEE Transactions on Industry Applications*, vol. 55, no. 5, pp. 4865–4875, 2019.

[21] D. Wu, F. Tang, T. Dragicevic, J. C. Vasquez, and J. M. Guerrero, "A control architecture to coordinate renewable energy sources and energy storage systems in islanded microgrids," *IEEE Transactions on Smart Grid*, vol. 6, no. 3, pp. 1156–1166, 2014.

[22] Y. Karimi, H. Oraee, and J. M. Guerrero, "Decentralized method for load sharing and power management in a hybrid single/three-phase-islanded microgrid consisting of hybrid source pv/battery units," *IEEE Transactions on Power Electronics*, vol. 32, no. 8, pp. 6135–6144, 2016.

[23] H. Mahmood and J. Jiang, "Decentralized power management of multiple pv, battery, and droop units in an islanded microgrid," *IEEE Transactions on Smart Grid*, vol. 10, no. 2, pp. 1898–1906, 2017.

[24] J. Jiang and C. Coates, "Power sharing scheme for an islanded microgrid including renewables and battery storage," in *2018 IEEE 4th Southern Power Electronics Conference (SPEC)*. IEEE, 2018, pp. 1–7.

[25] A. Azizi, S. Peyghami, H. Mokhtari, and F. Blaabjerg, "Autonomous and decentralized load sharing and energy management approach for dc microgrids," *Electric Power Systems Research*, vol. 177, p. 106009, 2019.

[26] P. D. Reigosa, H. Wang, Y. Yang, and F. Blaabjerg, "Prediction of bond wire fatigue of igbts in a pv inverter under a long-term operation," *IEEE Transactions on Power Electronics*, vol. 31, no. 10, pp. 7171–7182, 2016.

[27] D. G. Photovoltaics and E. Storage, "IEEE application guide for IEEE std 1547TM, IEEE standard for interconnecting distributed resources with electric power systems," 2009.

[28] N. Pogaku, M. Prodanovic, and T. C. Green, "Modeling, Analysis and Testing of Autonomous Operation of an Inverter-Based Microgrid," *IEEE Transactions on Power Electronics*, vol. 22, no. 2, pp. 613–625, Mar. 2007.

[29] J. He, Y. W. Li, J. M. Guerrero, F. Blaabjerg, and J. C. Vasquez, "An islanding microgrid power sharing approach using enhanced virtual impedance control scheme," *IEEE Transactions on Power Electronics*, vol. 28, no. 11, pp. 5272–5282, 2013.

[30] S. Peyghami, Z. Wang, and F. Blaabjerg, "A guideline for reliability prediction in power electronic converters," *IEEE Transactions on Power Electronics*, 2020.

[31] R. Bayerer, T. Herrmann, T. Licht, J. Lutz, and M. Feller, "Model for power cycling lifetime of igbt modules-various factors influencing lifetime," in *5th International Conference on Integrated Power Electronics Systems*. VDE, 2008, pp. 1–6.

[32] P. Asimakopoulos, K. Papastergiou, T. Thiringer, M. Bongiorno, and G. Le Godec, "On v_{ce} method: In situ temperature estimation and aging detection of high-current IGBT modules used in magnet power supplies for particle accelerators," *IEEE Transactions on Industrial Electronics*, vol. 66, no. 1, pp. 551–560, 2018.

[33] M. Musallam and C. M. Johnson, "An efficient implementation of the rainflow counting algorithm for life consumption estimation," *IEEE Transactions on Reliability*, vol. 61, no. 4, pp. 978–986, 2012.